High-quality Si_3N_4 circuits as a platform for graphene-based nanophotonic devices

N. Gruhler,[1] C. Benz,[1,3] H. Jang,[2] J.-H. Ahn,[2] R. Danneau,[1,3] and W. H. P. Pernice[1,*]

[1]*Institute of Nanotechnology, Karlsruhe Institute of Technology, 76344 Eggenstein-Leopoldshafen, Germany*
[2]*School of Electrical and Electronic Engineering, Yonsei University, Seoul 120-749, South Korea*
[3]*Institute of Physics, Karlsruhe Institute of Technology, D- 76049 Karlsruhe, Germany*
[*]*wolfram.pernice@kit.edu*

Abstract: Hybrid circuits combining traditional nanophotonic components with carbon-based materials are emerging as a promising platform for optoelectronic devices. We demonstrate such circuits by integrating single-layer graphene films with silicon nitride waveguides as a new architecture for broadband optical operation. Using high-quality microring resonators and Mach-Zehnder interferometers with extinction ratios beyond 40 dB we realize flexible circuits for phase-sensitive detection on chip. Hybrid graphene-photonic devices are fabricated via mechanical transfer and lithographic structuring, allowing for prolonged light-matter interactions. Our approach holds promise for studying optical processes in low-dimensional physical systems and for realizing electrically tunable photonic circuits.

OCIS codes: (130.3120) Integrated optics devices; (130.3130) Integrated optics materials; (230.5750) Resonators.

References and links

1. A. H. Castro Neto, N. M. R. Peres, K. S. Novoselov, and A. K. Geim, "The electronic properties of graphene," Rev. Mod. Phys. **81**(1), 109–162 (2009).
2. F. Bonaccorso, Z. Sun, T. Hasan, and A. C. Ferrari, "Graphene photonics and optoelectronics," Nat. Photonics **4**(9), 611–622 (2010).
3. A. A. Balandin, S. Ghosh, W. Bao, I. Calizo, D. Teweldebrhan, F. Miao, and C. N. Lau, "Superior thermal conductivity of single-layer graphene," Nano Lett. **8**(3), 902–907 (2008).
4. C. Lee, X. Wei, J. W. Kysar, and J. Hone, "Measurement of the elastic properties and intrinsic strength of monolayer graphene," Science **321**(5887), 385–388 (2008).
5. A. S. Mayorov, R. V. Gorbachev, S. V. Morozov, L. Britnell, R. Jalil, L. A. Ponomarenko, P. Blake, K. S. Novoselov, K. Watanabe, T. Taniguchi, and A. K. Geim, "Micrometer-scale ballistic transport in encapsulated graphene at room temperature," Nano Lett. **11**(6), 2396–2399 (2011).
6. R. Murali, Y. Yang, K. Brenner, T. Beck, and J. D. Meindl, "Breakdown current density of graphene nanoribbons," Appl. Phys. Lett. **94**(24), 243114 (2009).
7. K. S. Novoselov, A. K. Geim, S. V. Morozov, D. Jiang, Y. Zhang, S. V. Dubonos, I. V. Grigorieva, and A. A. Firsov, "Electric field effect in atomically thin carbon films," Science **306**(5696), 666–669 (2004).
8. K. S. Novoselov, D. Jiang, F. Schedin, T. J. Booth, V. V. Khotkevich, S. V. Morozov, and A. K. Geim, "Two-dimensional atomic crystals," Proc. Natl. Acad. Sci. U. S. A. **102**(30), 10451–10453 (2005).
9. R. Cheng, J. Bai, L. Liao, H. Zhou, Y. Chen, L. Liu, Y.-C. Lin, S. Jiang, Y. Huang, and X. Duan, "High-frequency self-aligned graphene transistors with transferred gate stacks," Proc. Natl. Acad. Sci. U. S. A. **109**(29), 11588–11592 (2012).
10. F. T. Vasko, "Saturation of interband absorption in graphene," Phys. Rev. B **82**(24), 245422 (2010).
11. F. Wang, Y. Zhang, C. Tian, C. Girit, A. Zettl, M. Crommie, and Y. R. Shen, "Gate-variable optical transitions in graphene," Science **320**(5873), 206–209 (2008).
12. K. F. Mak, M. Y. Sfeir, Y. Wu, C. H. Lui, J. A. Misewich, and T. F. Heinz, "Measurement of the optical conductivity of graphene," Phys. Rev. Lett. **101**(19), 196405 (2008).
13. R. R. Nair, P. Blake, A. N. Grigorenko, K. S. Novoselov, T. J. Booth, T. Stauber, N. M. R. Peres, and A. K. Geim, "Fine structure constant defines visual transparency of graphene," Science **320**(5881), 1308 (2008).
14. T. Ando, Y. Zheng, and H. Suzuura, "Dynamical conductivity and zero-mode anomaly in honeycomb lattices," J. Phys. Soc. Jpn. **71**(5), 1318–1324 (2002).
15. L. A. Falkovsky and A. A. Varlamov, "Space-time dispersion of graphene conductivity," Eur. Phys. J. B **56**(4), 281–284 (2007).

#195990 - $15.00 USD Received 19 Aug 2013; accepted 3 Dec 2013; published 13 Dec 2013

16. A. B. Kuzmenko, E. van Heumen, F. Carbone, and D. van der Marel, "Universal optical conductance of graphite," Phys. Rev. Lett. **100**(11), 117401 (2008).
17. J. Wu, M. Agrawal, H. A. Becerril, Z. Bao, Z. Liu, Y. Chen, and P. Peumans, "Organic light-emitting diodes on solution-processed graphene transparent electrodes," ACS Nano **4**(1), 43–48 (2010).
18. S. Bae, H. Kim, Y. Lee, X. Xu, J.-S. Park, Y. Zheng, J. Balakrishnan, T. Lei, H. R. Kim, Y. I. Song, Y.-J. Kim, K. S. Kim, B. Ozyilmaz, J.-H. Ahn, B. H. Hong, and S. Iijima, "Roll-to-roll production of 30-inch graphene films for transparent electrodes," Nat. Nanotechnol. **5**(8), 574–578 (2010).
19. C. D. Sheraw, L. Zhou, J. R. Huang, D. J. Gundlach, T. N. Jackson, M. G. Kane, I. G. Hill, M. S. Hammond, J. Campi, B. K. Greening, J. Francl, and J. West, "Organic thin-film transistor-driven polymer-dispersed liquid crystal displays on flexible polymeric substrates," Appl. Phys. Lett. **80**(6), 1088 (2002).
20. H. Li, Y. Anugrah, S. J. Koester, and M. Li, "Optical absorption in graphene integrated on silicon waveguides," Appl. Phys. Lett. **101**(11), 111110 (2012).
21. Q. Bao, H. Zhang, B. Wang, Z. Ni, C. H. Y. X. Lim, Y. Wang, D. Y. Tang, and K. P. Loh, "Broadband graphene polarizer," Nat. Photonics **5**(7), 411–415 (2011).
22. M. Furchi, A. Urich, A. Pospischil, G. Lilley, K. Unterrainer, H. Detz, P. Klang, A. M. Andrews, W. Schrenk, G. Strasser, and T. Mueller, "Microcavity-integrated graphene photodetector," Nano Lett. **12**(6), 2773–2777 (2012).
23. B. Y. Zhang, T. Liu, B. Meng, X. Li, G. Liang, X. Hu, and Q. J. Wang, "Broadband high photoresponse from pure monolayer graphene photodetector," Nat. Commun. **4**, 1811 (2013).
24. M. Liu, X. Yin, E. Ulin-Avila, B. Geng, T. Zentgraf, L. Ju, F. Wang, and X. Zhang, "A graphene-based broadband optical modulator," Nature **474**(7349), 64–67 (2011).
25. W. Bludau, A. Onton, and W. Heinke, "Temperature dependence of the band gap of silicon," J. Appl. Phys. **45**(4), 1846–1848 (1974).
26. N. Daldosso, M. Melchiorri, F. Riboli, F. Sbrana, L. Pavesi, G. Pucker, C. Kompocholis, M. Crivellari, P. Bellutti, and A. Lui, "Fabrication and optical characterization of thin two-dimensional Si3N4 waveguides," Mater. Sci. Semicond. Process. **7**(4–6), 453–458 (2004).
27. J. W. Suk, A. Kitt, C. W. Magnuson, Y. Hao, S. Ahmed, J. An, A. K. Swan, B. B. Goldberg, and R. S. Ruoff, "Transfer of CVD-grown monolayer graphene onto arbitrary substrates," ACS Nano **5**(9), 6916–6924 (2011).
28. K. S. Novoselov, A. K. Geim, S. V. Morozov, D. Jiang, M. I. Katsnelson, I. V. Grigorieva, S. V. Dubonos, and A. A. Firsov, "Two-dimensional gas of massless Dirac fermions in graphene," Nature **438**(7065), 197–200 (2005).
29. L. A. Falkovsky, "Optical properties of graphene," J. Phys. Conf. Ser. **129**, 012004 (2008).
30. F. H. L. Koppens, D. E. Chang, and F. J. García de Abajo, "Graphene plasmonics: A platform for strong light-matter interactions," Nano Lett. **11**(8), 3370–3377 (2011).
31. A. Gondarenko, J. S. Levy, and M. Lipson, "High confinement micron-scale silicon nitride high Q ring resonator," Opt. Express **17**(14), 11366–11370 (2009).
32. A. B. Matsko, *Practical Applications of Microresonators in Optics and Photonics* (CRC Press, 2009).
33. T. J. Kippenberg and K. J. Vahala, "Cavity opto-mechanics," Opt. Express **15**(25), 17172–17205 (2007).
34. K. Hennessy, A. Badolato, M. Winger, D. Gerace, M. Atatüre, S. Gulde, S. Fält, E. L. Hu, and A. Imamoğlu, "Quantum nature of a strongly coupled single quantum dot-cavity system," Nature **445**(7130), 896–899 (2007).
35. J. Čtyroký, I. Richter, and M. Šiňor, "Dual resonance in a waveguide-coupled ring microresonator," Opt. Quantum Electron. **38**(9–11), 781–797 (2007).
36. M. Gorodetsky, A. Pryamikov, and V. Ilchenko, "Rayleigh scattering in high-Q microspheres," J. Opt. Soc. Am. B **17**(6), 1051–1057 (2000).
37. J. F. Bauters, M. J. Heck, D. John, D. Dai, M. C. Tien, J. S. Barton, A. Leinse, R. G. Heideman, D. J. Blumenthal, and J. E. Bowers, "Ultra-low-loss high-aspect-ratio Si3N4 waveguides," Opt. Express **19**(4), 3163–3174 (2011).
38. M.-C. Tien, J. F. Bauters, M. J. R. Heck, D. T. Spencer, D. J. Blumenthal, and J. E. Bowers, "Ultra-high quality factor planar Si3N4 ring resonators on Si substrates," Opt. Express **19**(14), 13551–13556 (2011).
39. Y. Lee, S. Bae, H. Jang, S. Jang, S.-E. Zhu, S. H. Sim, Y. I. Song, B. H. Hong, and J.-H. Ahn, "Wafer-scale synthesis and transfer of graphene films," Nano Lett. **10**(2), 490–493 (2010).
40. J. Gosciniak and D. T. H. Tan, "Graphene-based waveguide integrated dielectric-loaded plasmonic electro-absorption modulators," Nanotechnology **24**(18), 185202 (2013).
41. Z. Lu and W. Zhao, "Nanoscale electro-optic modulators based on graphene-slot waveguides," J. Opt. Soc. Am. B **29**(6), 1490–1496 (2012).

1. Introduction

Graphene, a strictly two-dimensional material consisting of carbon atoms arranged in a honeycomb lattice, has many remarkable electronic [1], optical [2], thermal [3], and mechanical [4] properties. Especially the combination of unique electronic and optical properties is very promising for applications in high-frequency, broadband optoelectronic devices. Based on the high charge carrier mobility [5], the ultra-high current sustainability [6], and the strong field-effect-transistor behavior [7,8], high-frequency graphene transistors with a cutoff frequency of 427 GHz have been reported [9] paving the road towards ultrafast

#195990 - $15.00 USD Received 19 Aug 2013; accepted 3 Dec 2013; published 13 Dec 2013

devices. However, enhanced functionality can be realized by not only controlling the electronic properties but also the optical properties as a viable route to fabricate high-speed optoelectronic devices. Among graphene's extraordinary optical properties are its nonlinear saturable absorption [10], electrically controlled interband excitations [11], and an almost constant optical absorption coefficient in the spectral range from visible to infrared wavelengths [12,13]. Being the reasons for graphene's unique electronic properties, the flat absorbance spectrum is also caused by the conical energy dispersion around the Dirac points. Considering only interband transitions close to these points in undoped graphene a universal optical conductivity of $e^2/\hbar$ is obtained [14,15]. By applying Fresnel equations in the thin film limit, the absorbance of a freestanding graphene monolayer is derived to be $\pi\alpha \approx 2.3\%$ [13,16], with the fine structure constant α. This value is obtained in the case of normal incident of light. Because the absorption coefficient is relatively small, graphene can be used to realize transparent charge injecting electrodes in OLEDs [17] or as flexible, transparent, conducting films in touch screens [18], smart windows, and bistable displays [19].

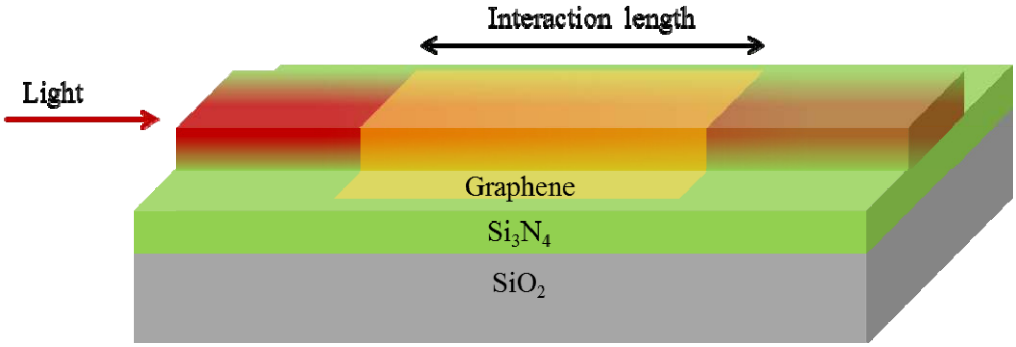

Fig. 1. A graphene layer is placed on top of a partially etched Si_3N_4 rib waveguide on a silica substrate. Therefore, the light-graphene interaction length is limited only by the length of the graphene layer and a large amount of light propagating along the waveguide is absorbed.

However, for many applications strong light-graphene interaction is required in order to optimize and tailor device performance. This can be achieved by integrating graphene in nanophotonic circuits [20] so that light travels along the graphene layer. Here we adopt this approach for hybrid graphene-silicon nitride waveguiding devices. The prototype configuration is shown in Fig. 1: a graphene layer is placed on top of a partially etched Si_3N_4 rib waveguide on a silica substrate. The light-graphene interaction length is decoupled from the minimal graphene thickness and is only limited by the length of the hybrid waveguide. Thus, an arbitrary amount of light can be absorbed with a well-chosen length.

Using such a parallel arrangement of graphene and a waveguide or a fiber, a number of graphene-based optoelectronic devices have been demonstrated including polarization controllers [21], photodetectors [22,23], and optical modulators [24]. By applying a gate voltage to a graphene flake on top of a waveguide the interband transitions are controlled and a modulation of the attenuation coefficient of the mode in the waveguide with a 3 dB bandwidth of 10 GHz has been achieved [24]. To date, predominantly silicon waveguides have been used for the fabrication of such structures. However, silicon waveguides are restricted to operation wavelengths above 1100 nm due to the relatively small bandgap of 1.1 eV [25].

Here we instead implement graphene-based nanophotonic devices on a Si_3N_4 platform. Si_3N_4 provides low material absorption even for visible wavelengths [26] and is therefore a suitable material to take advantage of the broadband flat absorption of graphene. Thus, the operation wavelength of graphene based nanophotonic devices can be extended beyond

#195990 - $15.00 USD Received 19 Aug 2013; accepted 3 Dec 2013; published 13 Dec 2013

infrared wavelengths usually within the C-band around 1550 nm, to visible or even ultraviolet wavelengths. A robust fabrication procedure employing controlled reflow of ebeam resist is used to obtain high quality nanophotonic circuits with propagation loss below 21 dB/m. Ring and racetrack resonators with high quality factors ($1.6\text{x}10^6$) and Mach-Zehnder interferometers (MZIs) with high extinction ratio above 40 dB are fabricated and both can be used as phase and amplitude sensitive devices. Moreover, the fabrication of the nanophotonic Si_3N_4 circuits as well as the graphene flakes is compatible with standard CMOS processing. Because graphene can be produced at the wafer scale [18], transferred onto arbitrary substrates [27] and patterned into planar devices [28], our approach holds promise for large area hybrid carbon-photonic devices for optoelectronic and tunable photonic applications.

2. Simulations

The optical absorption of graphene can be described in terms of the optical conductivity σ. It consists of two parts, the intraband and interband excitations, and can be derived within the random phase approximation [29,30] depending on the frequency ω, chemical potential μ, temperature T, and scattering time τ to be

$$\sigma(\omega,\mu,T,\tau) = \sigma^{\text{intra}}(\omega,\mu,T,\tau) + \sigma^{\text{inter}}(\omega,\mu,T,\tau)$$
$$= \frac{e^2}{\hbar}\frac{2ik_BT}{\pi\hbar\left(\omega+i\tau^{-1}\right)}\ln\left(2\cosh\left(\frac{\mu}{2k_BT}\right)\right) + \frac{e^2}{\hbar}\left(G\left(\frac{\hbar\omega}{2}\right) - \frac{4\hbar\omega}{i\pi}\int_0^\infty \frac{G(\varepsilon)-G(\hbar\omega/2)}{\hbar^2\omega^2-4\varepsilon^2}\,\mathrm{d}\varepsilon\right),$$

where

$$G(\varepsilon) = \frac{\sinh(\varepsilon/k_BT)}{\cosh(\mu/k_BT)+\cosh(\varepsilon/k_BT)}.$$

A shift of the chemical potential of half of the photon energy prevents interband transitions due to Pauli blocking or no available electrons depending on the direction of the shift. Here by assigning a finite thickness to the graphene layer, the optical conductivity is used to calculate the complex refractive index of the graphene layer, which in turn is used for FEM simulations of a waveguide with a graphene layer on top of it in order to obtain the effective refractive index of the waveguide mode and the attenuation coefficient. The simulations are employed for a first approximation of the absorption coefficient in a photonic waveguide, where FEM methods are traditionally used tools. In this case using a finite thickness for the graphene layer is a necessity due to limited numerical resolution. Here we reduce the thickness until no further change in the effective refractive index occurs and the numerical results converge towards a given value. However, despite the rather coarse approximation the predictions turn out to correspond closely to the experimental values as described further below.

The simulations are carried out for a temperature of $T = 300\,\text{K}$, $\tau = 10^{-13}\,\text{s}$ [30], $\lambda = 1550\,\text{nm}$ and the 330 nm Si_3N_4 layer on SiO_2 is half etched to a 165 nm rib waveguide. The profile of a mode propagating along such a configuration is shown in Fig. 2(a)). When the chemical potential is not shifted from the neutrality point, an attenuation of $\alpha = 0.066\,\text{dB}/\mu\text{m}$ is obtained. The resultant behavior of the attenuation coefficient and the group index when the chemical potential is shifted is shown in Fig. 2(b)). The attenuation coefficient exhibits a step like behavior when interband transitions are prevented due to a shift of the chemical potential. At $\mu = 0.4\,\text{eV}$, which corresponds to half the photon energy, the curve is steepest. At the same point the group index exhibits a small maximum and decreases then with increasing chemical potential. With this variation of the attenuation coefficient and the group index, graphene-based devices like optical modulators can be fabricated on a Si_3N_4 photonics platform.

#195990 - $15.00 USD Received 19 Aug 2013; accepted 3 Dec 2013; published 13 Dec 2013

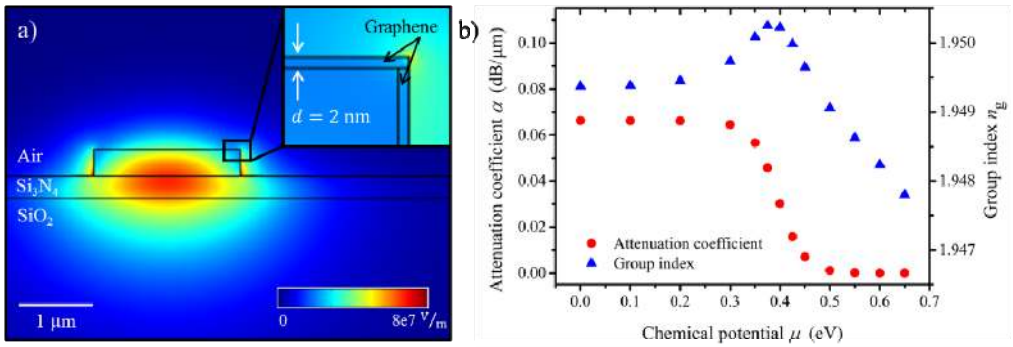

Fig. 2. a) Mode profile of the fundamental TE-like mode in a Si_3N_4 rib waveguide with a graphene layer on top of it. The inset shows a close-up of the graphene layer. b) When the chemical potential is shifted, the attenuation coefficient shows a step-like behavior because interband excitations are prevented. However, due to thermal excitation this step is broadened. Additionally to the attenuation coefficient, the group index of the mode also changes. It exhibits a small maximum before it decreases with increasing chemical potential.

3. Substrate preparation and device fabrication

To experimentally verify the absorption properties of graphene-Si_3N_4 devices we design several nanophotonic circuits. For the fabrication of the circuits, silicon carrier wafers are thermally oxidized to a thickness of 3.3 µm to provide an optical buffer layer with lower refractive index (1.45) compared to silicon nitride. Subsequently a 330 nm thick stoichiometric Si_3N_4 layer is grown on the wafer using low pressure chemical vapour deposition (LPCVD). These films contain high tensile stress, yielding a refractive index of $n = 2.00 \pm 0.02$. Photonic devices are then patterned using a 50 kV JEOL JBX-5500ZD electron beam lithography system. Negative tone ma-N 2403 resist with a thickness of 340 nm is employed to create a mask which provides sufficient protection for subsequent dry etching.

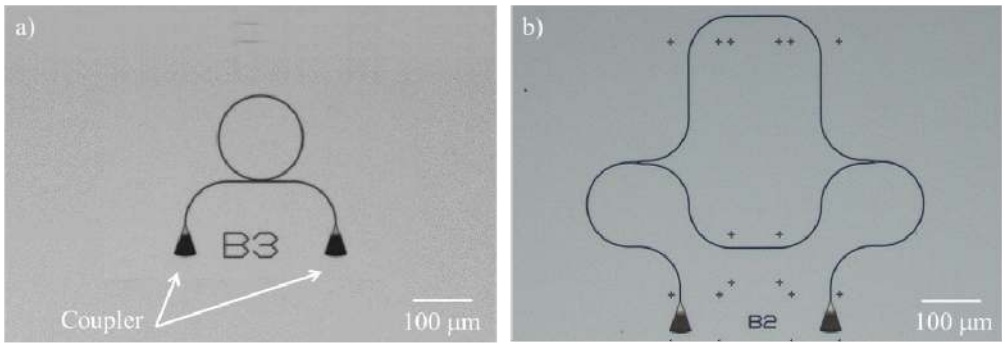

Fig. 3. Optical micrograph of a ring resonator coupled to a bus waveguide (a) and of a Mach-Zehnder interferometer (b). The black triangles visible at the bottom of the images are apodized focusing grating couplers, which are used to couple light into and out of the nanophotonic circuit.

After the development step a reflow procedure is applied, which greatly increases the quality of the fabricated devices due to decreased surface roughness of the resist [31]. The reflow process consists of an additional baking step on a hotplate which causes the resist to become soft enough for the surface tension to plastically deform the polymer. For ma-N 2403 it was observed that the resist shrinks at the top by 1-10% depending on the temperature and the resist thickness [31], while the bottom surface of the resist remains attached to the nitride. Thereby the residual roughness of the resist is greatly reduced which translates into smoother

#195990 - $15.00 USD Received 19 Aug 2013; accepted 3 Dec 2013; published 13 Dec 2013

sidewalls of the waveguides after etching. In our case, different reflow temperatures are used depending on the device layout. In Fig. 3 two devices, a MZI (a) and a ring resonator coupled to a bus waveguide (b) are shown. In order to split the waveguide into two arms for the interferometer, a Y-splitter with a very fine tip is used, while the ring resonator circuit does not exhibit such fine structures. Therefore a lower reflow temperature has to be used for the MZIs in order to avoid deformation of the fine tip of the splitter. After the reflow the circuits are transferred into the Si_3N_4 layer via reactive ion etching. CHF_3/O_2 chemistry is used for the etching step in an Oxford 80 Plasmalab system. Afterwards the resist is removed by O_2 plasma ashing.

4. High quality / phase sensitive devices

In order to measure small changes in the group index or attenuation coefficient of a waveguide mode coupled to a graphene top layer, it is necessary to fabricate circuits with very low propagation losses. Especially MZIs are very useful for measuring the attenuation of waveguide-graphene structures, while both rings and MZIs can be used to enhance the modulation depth of a graphene-based optical modulator. Moreover, ring resonators cannot only be used as filters and many other applications but are also handy tools to quantitatively measure the scattering loss of fabricated waveguides. The optical quality factor of a ring resonator is directly related to the propagation loss in the waveguide and therefore can be used to find optimal parameters for the fabrication process and the waveguide geometry. In this work the 330 nm thick Si_3N_4 layer is half etched, leading to a 165 nm high rib waveguide as sketched schematically in Fig. 1. The waveguide width is chosen to be 1.15 µm, which is just below the cutoff width of the second mode, so that it is still a single mode waveguide but the overlap of the field of the mode with the sidewall is reduced. This is important as the surface roughness of the waveguide is the main source of propagation losses.

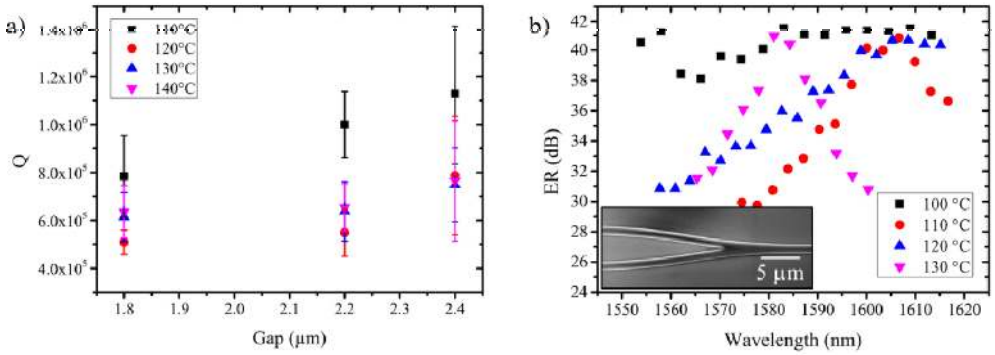

Fig. 4. Comparison of different reflow temperatures. a) For ring resonators a reflow temperature of 110 °C yields the highest Q-factors. b) The Y-splitters (see inset) in MZIs exhibit a very fine tip, which is endangered in the reflow process. Therefore, with a lower temperature of 100 °C the best results are achieved. The ER of the MZI exhibits a flat behavior exceeding 40 dB over a spectral range between 1550 - 1620 nm.

In order to find the best reflow parameters several samples were prepared by e-beam lithography and heated up for 2 min on a hotplate to temperatures between 100 and 145 °C. Then the samples were etched and the resulting quality factors of the rings and extinction ratios of MZI devices were compared. The results for four different reflow temperatures are shown in Fig. 4. In Fig. 4(a)) the quality factors of ring resonators with a gap between the ring and the bus waveguide up to 2.4 µm are presented. For these gap sizes the rings are very weakly coupled to the bus waveguide and thus the resulting quality factor is close to the intrinsic Q-factor of the ring (which is directly related to the propagation loss). The radius of the rings is kept at 70 µm. Without a reflow process the rings exhibited quality factors around

#195990 - $15.00 USD Received 19 Aug 2013; accepted 3 Dec 2013; published 13 Dec 2013

10^5 (not shown). The introduction of the reflow process increases the Q-factor by one order of magnitude to values exceeding 10^6. In Fig. 4(a)) each data point represents the average Q-factor of one device. For the calculation of the average Q-factor ten to fifteen resonances of one device are measured and the error bars show the standard deviation of these resonances from the mean value. The highest Q-factor is achieved with a reflow process at 110 °C for two minutes. For both, higher and lower temperatures, the quality factors decrease due to higher losses.

However, it is important to optimize the reflow procedure not only regarding the waveguide losses but also with respect to preserving finer structures. Therefore, the reflow procedure is also tested for MZIs. These devices contain Y-splitters, which consist of a taper region where the waveguide width is doubled before it is split into two waveguides with the original width. Such a Y-Splitter is shown in the inset of Fig. 4. The very fine tapered tip of this splitter is remolded during the reflow process; sharp edges become rounder. It is crucial that the power of a mode is equally divided by such a structure even when a reflow process is applied. The extinction ratio of a MZI between the maximum output power for constructive interference and minimum output power for destructive interference depends highly on the splitting ratio of the Y-splitter. For a 50:50 splitting ratio the ER becomes maximal. By applying a wavelength sweep, a typical interference spectrum is obtained for the transmitted optical power (not shown). Here we use MZIs, for which one of the interferometer arms is 400 µm longer than the other. For each interference fringe, the extinction ratio is calculated, which is shown in Fig. 4(b)) for the different reflow temperatures. The best performance of the splitter was realized with a reflow process at 100 °C (slightly lower compared to the optimal temperature for ring devices). The ER is approximately stable for all wavelengths between 1550 nm and 1620 nm at a very high value exceeding 40 dB. All devices fabricated at higher temperatures exhibit such high ER only for a certain wavelength and the ER decreases rapidly for other wavelengths. Most likely, at the point of the splitter, the mode exhibits a profile which is split equally only for a certain wavelength, while it is split asymmetrically for all other wavelengths. Therefore, a reflow process at 110 °C is used for circuits without fine structures, while 100 °C is used, if the circuits contain Y-splitters or other fine features.

Ring resonators are not only useful to compare different waveguide geometries or fabrication procedures but especially resonators with very high quality factors are of much interest themselves [32–34]. Using the fabrication procedure described above, high-Q ring resonators are fabricated. The waveguide width is set to 1.15 µm, the Si_3N_4 layer is half etched to 165 nm, and the ring radius is varied in order to obtain resonators with a radius large enough so that bending losses can be neglected. The resulting quality factors with increasing gap for different ring radii are shown in Fig. 5(a)). With increasing gap between ring and bus waveguide the coupling losses play a decreasing role, which leads to increasing Q-factors. While bending losses lead to low Q-factors for radii of 40 µm and 70 µm, no further increase in the Q-factors is detected for ring radii larger than 100 µm. The highest Q-factors are obtained for a ring resonator with a radius of 140 µm at a gap of 2.2 µm. The average Q-factor of this resonator is 1.3×10^6 and three of the resonances exhibit Q-factors exceeding 1.6×10^6. These Q-factors correspond to propagation losses of 26 dB/m and 21 dB/m respectively. One of the resonances with the highest Q-factors is shown in Fig. 5(b)). However, not a single resonance dip but mode splitting of the resonance is obtained.

#195990 - $15.00 USD Received 19 Aug 2013; accepted 3 Dec 2013; published 13 Dec 2013

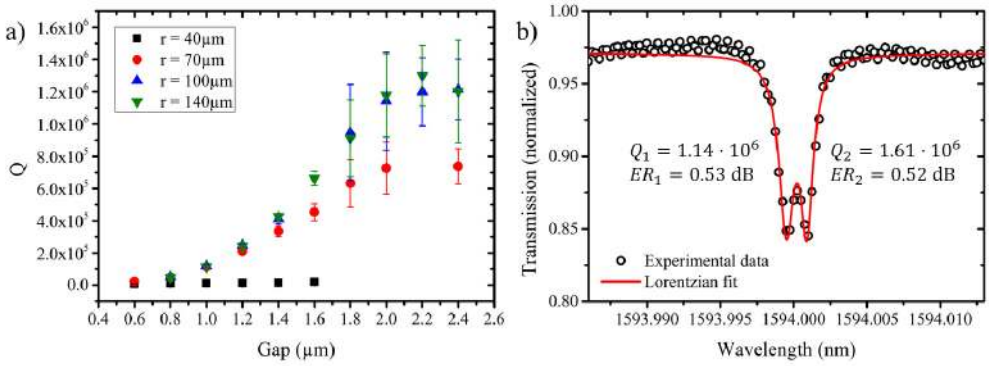

Fig. 5. a) Measured Q-factors of ring resonators with radii up to 140 µm. For a radius larger than 100 µm no further increase in Q was observed. Rings with a radius of 40 µm exhibit high bending losses such that the increase of the Q-factor with gap size is too low to be seen on this scale. The highest Q-factor is achieved for a ring with a radius of 140 µm at a gap of 2.2 µm. One resonance of this resonator is shown in b). Due to coupling of the clockwise and counterclockwise propagating mode in the ring, the resonance is split into two dips.

Due to coupling of the clockwise and counterclockwise propagating mode in the ring, caused for instance by surface roughness, splitting of the resonance into two dips is obtained [35,36]. Moreover, this resonator exhibits still 85% transmission on resonance and thus, the intrinsic quality factor of the resonator is not yet obtained. The propagation losses achieved here are comparatively low, especially because no sophisticated fabrication steps or special waveguide geometries with large bending radii have to be used. In the C-band at a wavelength of 1550 nm Si_3N_4 waveguides with a propagation loss of 3 dB/m at 2 mm bend radius and 8 dB/m at 0.5 mm bend radius have been previously demonstrated [37]. In [38] ring resonators with quality factors of 7×10^6 at a much larger bend radius of 2 mm have been presented, corresponding to propagation losses of 2.9 dB/m. However, in both cases the waveguide core had been completely surrounded by a SiO_2 cladding, which would lead to weaker graphene-waveguide interaction because of a larger separation between the optical mode and the graphene layer.

5. Hybrid graphene-nanophotonic devices

The above described fabrication procedure is then used to fabricate low-loss nanophotonic circuits. Both, high-Q ring resonators and MZIs can be used to detect small changes in the phase or amplitude of a waveguide mode with a high sensitivity and are therefore well suitable for the characterization of a waveguide-graphene structure. The first step for building photonic devices based on graphene is to determine the strength of the graphene-light interaction. A measure of this is the absorption of light propagating along a waveguide on which graphene was transferred. For the fabrication of waveguide-graphene structures, CVD graphene transferred to silicon carrier substrates is used. A detailed description of the fabrication and transfer procedure can be found in [18, 39]. Via Raman spectroscopy we confirmed that graphene monolayers are used in fact for the fabrication of the devices. For the transfer of the graphene onto a waveguide, a Si carrier wafer is spin coated with PMMA which attaches to the graphene. The carrier wafer is then dipped into DI water to release the PMMA/graphene layer, leaving it floating on the water surface. The PMMA/graphene stack can then be placed on a transfer plate which is heated to adhere and straighten the PMMA/graphene layer. After aligning the transfer plate to the heated target chip containing the nanophotonic circuits, both are brought into close proximity. Upon contact, the PMMA attaches to the target substrate while increasing the heat leads to uniform adhesion of the graphene. A large CVD graphene layer is used in order to cover many devices at the same time. For structuring the graphene layer to a desired shape, another e-beam lithography step is

#195990 - $15.00 USD Received 19 Aug 2013; accepted 3 Dec 2013; published 13 Dec 2013

used to fabricate a PMMA etching mask. Graphene shall remain only at a specific position with a well-defined shape on the waveguides and therefore a window is written in the PMMA layer above the rest of the circuits. Then a low-power O_2 RIE process is used for etching the graphene in the open areas.

In order to measure the attenuation coefficient of a waveguide-graphene structure, graphene is placed on one of the two arms of the MZIs. The design of such a configuration is shown in Fig. 6(a)). The arms of the MZI exhibit a length difference ΔL and on the longer of the two MZI arms a graphene flake with length l is placed.

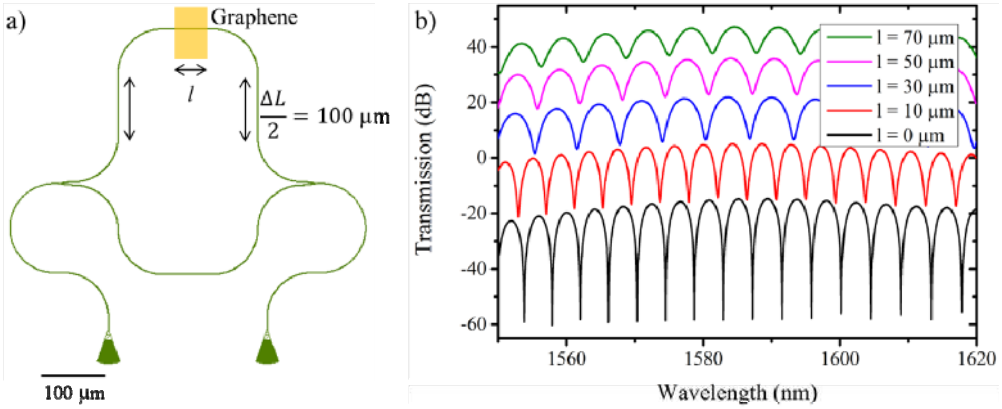

Fig. 6. a) Design of a MZI on which a graphene layer with length l has been transferred. b) Transmission curves of MZIs in which graphene flakes with varying length have been transferred. With increasing length the ER decreases from 40 dB (without graphene) to less than 10 dB (with a 70 µm long graphene flake).

As the simulated attenuation coefficient of the waveguide-graphene structure (0.066 dB/µm) is much larger than the loss of the waveguide itself (2.1×10^{-5} dB/µm), the propagation losses of the waveguide can be neglected when the output power of such a MZI is derived. When measuring in transmission the output power at the exit waveguide of the MZI is given as

$$P_{\text{out}} = \frac{1}{4} P_{\text{in}} \left(1 + e^{-\alpha l} + 2e^{-\alpha l} \cos\left(\frac{2\pi}{\lambda} \left(n_{\text{g}} \Delta L + \Delta n_{\text{g}} l \right) \right) \right), \tag{5.1}$$

where α is the attenuation coefficient of the waveguide-graphene structure, λ is the wavelength, n_{g} is the group index of the mode propagating along the waveguide without graphene on top of it and Δn_{g} is the deviation of the group index when graphene is placed on top of the waveguide from its initial value. From this equation, the extinction ratio (ER) between maximum and minimum output power can be derived to be:

$$ER = \frac{P_{\text{out,max}}}{P_{\text{out,min}}} = \left(\frac{1 + e^{-\alpha l/2}}{1 - e^{-\alpha l/2}} \right)^2 . \tag{5.2}$$

The ER is directly related to the attenuation coefficient and can therefore be used to determine the attenuation coefficient from a simple transmission measurement without the difficulty of determining the absolute input and output power levels before and after the graphene transfer.

For an accurate determination of the attenuation coefficient, many devices with varying length of the graphene flake are fabricated. The length is varied between 10 µm and 70 µm in 10 µm steps. For each MZI the transmission spectrum is recorded and the ER calculated. An exemplary set of recorded transmission curves with increasing length of the graphene flake is

#195990 - $15.00 USD Received 19 Aug 2013; accepted 3 Dec 2013; published 13 Dec 2013

presented in Fig. 6(b)). As expected from Eq. (5.2), the ER decreases with increasing length of the graphene flake. Without graphene an ER of 40 dB is obtained, which decreases to approximately 20 dB for a 10 µm long graphene flake and below 10 dB for a 70 µm long flake. The difference in the FSR of the interference pattern between the two curves at the bottom and the other ones is caused by a designed length difference of the interferometer arms. For the two devices with a smaller FSR the length difference was set to $\Delta L = 300$ µm and for the other devices to $\Delta L = 200$ µm. The dependence of the absorption coefficient on the length of the graphene flake is presented in Fig. 7.

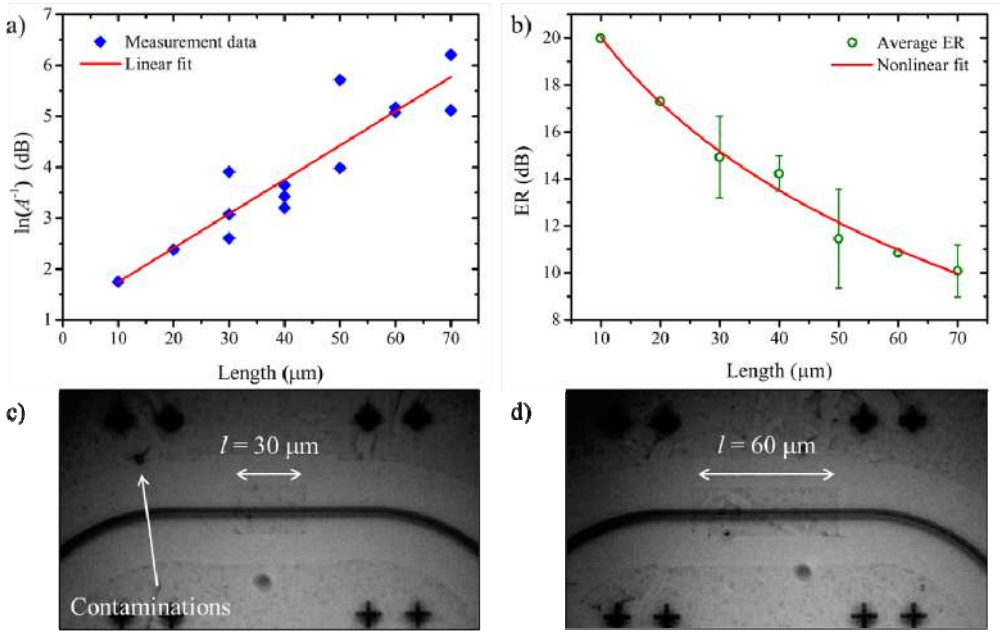

Fig. 7. a) Data plot of the ER of MZIs depending on the length of the graphene flake placed on one of the MZI arms. b) The ER decreases accordingly to Eq. (5.2). c), d) Optical micrographs of a CVD graphene layer patterned into a 30 µm and 60 µm long flake respectively. Together with the graphene layer there are also some contaminating particles transferred onto the sample.

The attenuation $A = e^{-\alpha l}$ which is plotted in Fig. 7(a)) can be obtained from the ER shown in Fig. 7(b)). As expected the attenuation shows a linear behavior with increasing graphene length. However, due to damaging of the waveguide during the fabrication and because some graphene flakes are ripped off when the PMMA mask is dissolved, the number of data points per length of the graphene flake varies. The attenuation coefficient is extracted from a linear fit to the data in Fig. 7(a)) as

$$\alpha = (0.067 \pm 0.008)\ \text{dB/µm}$$

which is in very good agreement with the simulations. During the fit a constant offset is allowed for the attenuation which amounts to

$$y_0 = (1.07 \pm 0.4)\ \text{dB}.$$

The offset of the attenuation can be caused by several different effects: even without graphene the ER of the devices is finite due to imperfect beam splitting and small propagation losses in the waveguide. The average ER of the devices before graphene is transferred onto them was 38 dB, which corresponds to a y-offset of 0.22 dB for the attenuation coefficient.

#195990 - $15.00 USD Received 19 Aug 2013; accepted 3 Dec 2013; published 13 Dec 2013

Additionally, the graphene layer is put on the longer of the two interferometer arms and on this arm it is more likely that some dust particles are transferred to it which causes an increase the attenuation coefficient. Moreover, light is not only absorbed by the graphene layer but also back-scattered at the beginning of the flake which leads to an additional offset of the attenuation coefficient. In Figs. 7(c) and 7(d) two graphene flakes are shown after they have been patterned into the desired shape. The transferred CVD graphene layer initially covered many devices but during the fabrication it was etched away along the waveguide apart from one specific spot. In the pictures some contaminating particles, which have been transferred onto the sample together with the graphene layer, can be seen. If these particles land on the waveguide and are too large so that they are not etched away in the oxygen plasma, they cause additional absorption.

For a graphene layer on a Si waveguide an attenuation coefficient between 0.1 dB/μm and 0.14 dB/μm has been reported with the prospect of increasing up to 0.2 dB/μm [24,39]. Especially with a waveguide geometry that supports a TM-like mode which exhibits a high field amplitude at the top interface of the waveguide the graphene-light interaction strength can be increased. Additionally it has been proposed to enhance the interaction strength by placing two graphene layers and a spacer between a thin metal film and a dielectric in order to obtain graphene-absorption in a dielectric-loaded surface plasmon polariton waveguide in which the metal film is connected to one of the graphene layers as a control electrode for modulations of the absorption [40]. Another proposal is to place graphene in the middle of a Si_3N_4 sandwich structure at the maximum of the field amplitude of the mode propagating along the waveguide [41]. Additionally the waveguide is covered by a Cu or Si cladding. However, for the realization of the proposed structures more advanced lithography, material deposition and structuring steps are necessary than for the approach chosen here.

Additionally to the MZIs, graphene is also transferred onto five racetrack resonators and patterned into 10 μm long flakes. Before the graphene layer was transferred onto the devices, the racetrack resonators exhibited a quality factor of approximately 440,000 and were near-critically coupled. After graphene had been transferred onto the resonator and structured to a 10 μm long flake the quality factors decreased to 24,000 and the resonators were weakly coupled with an ER of only 0.4 dB. This reduction of the quality factor is slightly more significant than expected. Applying the data obtained by the absorption measurement a quality factor around 38,000 would have been expected even when the offset of the attenuation coefficient is taken into account. The further reduction of the quality factor can be explained by two effects. Back-scattering at the beginning of the graphene flake becomes more important than for MZIs because light is passing the graphene flake not only once but multiple times. Moreover in a MZI perturbations of the waveguide are partly compensated if the two arms are equally disturbed. For a racetrack resonator however no such compensation can occur and all contaminating particles lead to a further reduction of the quality factor due to higher propagation losses. After graphene is transferred onto a racetrack resonator, the coupling losses play a minor role compared to the increased propagation losses and thus, the resonators are no longer critically but weakly coupled with a much lower ER.

6. Conclusions

We have demonstrated high-quality Si_3N_4 nanophotonic circuits which are used for the realization of graphene-based devices. The fabrication procedure and waveguide geometry have been optimized, resulting in ring resonators with Q-factors up to 1.6×10^6. This corresponds to a propagation loss of 21 dB/m. Mach-Zehnder interferometers with an extinction ratio exceeding 40 dB have been used to determine the attenuation coefficient of a waveguide-graphene hybrid structure as $\alpha = 0.067$ dB/μm in very good agreement with the simulations. Our fabrication procedure for the waveguide and the integration of the graphene layer avoids sophisticated processing steps and thus leads to high device yield. The hybrid graphene-Si_3N_4 nanophotonic platform introduced here can also be used for the realization of

#195990 - $15.00 USD Received 19 Aug 2013; accepted 3 Dec 2013; published 13 Dec 2013

electro-optic modulators. Furthermore, because Si_3N_4 provides a large electronic bandgap the operation bandwidth of such devices can be extended from infrared to visible and even UV wavelengths.

Acknowledgments

W.H.P. Pernice acknowledges support by DFG grant PE 1832/1-1 and PE 1832/1-2. We also acknowledge support by the Deutsche Forschungsgemeinschaft (DFG) and the State of Baden-Württemberg through the DFG-Center for Functional Nanostructures (CFN) within subproject A6.4. R.D.'s Shared Research Group SRG 1-33 received financial support by the Karlsruhe Institute of Technology within the framework of the German Excellence Initiative and by the EU project MMM@HPC FP7-261594. The authors wish to thank Silvia Diewald for assistance in device fabrication. We acknowledge support by the Deutsche Forschungsgemeinschaft and the Open Access Publishing Fund of the Karlsruhe Institute of Technology.